Experimental and numerical investigation of flame stabilization and pollutant formation in matrix stabilized ammonia-hydrogen combustion

Guillaume Vignat [a,*], Thorsten Zirwes [a,b,c], Edna R. Toro [a], Khaled Younes [a], Emeric Boigné [a], Priyanka Muhunthan [a], Lauren Simitz [d], Dimosthenis Trimis [c], Matthias Ihme [a,e]

[a] *Department of Mechanical Engineering, Stanford University, Stanford, CA 94305, USA*
[b] *Steinbuch Center for Computing, Karlsruhe Institute of Technology, Eggenstein-Leopoldshafen 76344, Germany*
[c] *Engler-Bunte-Institute, Division of Combustion Technology, Karlsruhe Institute of Technology, Karlsruhe 76131 Germany*
[d] *Department of Aeronautics and Astronautics, Stanford University, Stanford, CA 94305, USA*
[e] *Department of Photon Science, SLAC National Accelerator Laboratory, Menlo Park, CA 94025, USA*

A R T I C L E   I N F O

A B S T R A C T

Ammonia (NH_3) is a carbon-free fuel that offers an attractive alternative for reducing greenhouse gas emissions. However, the slow flame speed, low heating value, and emissions of nitrogen-containing pollutants present significant issues for practical combustion applications. To address these issues, we investigate the use of matrix stabilized combustion. In this type of burner, combustion is performed within an inert porous ceramic foam, heat is recirculated by solid conduction and radiation, which enhances flame speed and combustion stabilization, thereby permitting combustion over a wide range of equivalence ratio conditions. We present a new porous media burner (PMB) capable of stabilizing NH_3/air flames at ambient conditions. An extensive experimental characterization of the stability of this burner is conducted with up to 30% by volume of hydrogen (H_2) in the fuel stream. A 15:1 turndown ratio is demonstrated, with a high thermal power density of 62 MW m^{-3}. Concentrations of NO, unburnt NH_3, and H_2 in the exhaust stream are measured. Two regimes are identified for low NO operation: rich and very lean. For rich conditions, NO emissions decrease with increasing equivalence ratio and decreasing H_2 blending. Unburnt NH_3 emissions follow opposite trends. These measurements are complemented by simulations in which the burner is represented by a coupled solid-gas reactor network. This model captures the burner's pollutant emissions to good accuracy and is used to analyze the mechanisms of pollutant formation.

1. Introduction

The need to reduce anthropogenic emissions of greenhouse gases is driving the rapid transition towards carbon-free fuels [1]. Ammonia (NH_3), as a storable and energy-dense hydrogen (H_2) carrier, is an attractive option for applications in energy systems, industrial processes, and transportation [2,3]. After being produced in a low-carbon process, either using conventional methods with carbon capture and storage ("blue NH_3") or directly from clean electricity ("green NH_3"), NH_3 can be inexpensively transported over long distances using an already existing infrastructure, to be used in a number of applications. In the present work, we focus on its use as an energy source for industrial heating, boilers, and electricity production using gas turbines.

An overview of recent research concerned with burner design for NH_3 utilization can be found in Valera-Medina et al. [4], Kobayashi et al. [5], Elbaz et al. [6]. The combustion of NH_3 introduces several challenges, including low laminar flame speeds [7], long ignition delay times [8], low thermal power densities, and high emission levels of several nitrogen-containing pollutants (unburnt NH_3, N_2O, NO, NO_2) [9–11]. It has been shown that blending H_2 with NH_3 can enhance its combustion properties and alleviate some of the issues regarding flame stabilization [7,12]. Swirling injectors have been proposed to stabilize NH_3/H_2/air flames over a wide range of operating conditions: from very lean ($\phi \approx 0.3$) to rich ($\phi \approx 1.4$) equivalence ratios [10,12], with varying levels of H_2 addition [9,10,12,13], over a wide range of operating pressures [9,14], and with steam addition [15]. Several studies have suggested that, for minimal NO emissions, burners should be operated

at high pressure with equivalence ratios larger than $\phi \gtrsim 1.1$ [4,6]. However, when operating at these fuel-rich conditions, it becomes necessary to adopt a multistage burner design to reduce unburnt NH_3 emissions. NO emissions between 10 and 500 ppmv (normalized to 15% O_2) have been reported in the literature for high-pressure Rich-Quench-Lean combustors with steam addition [9,14]. In contrast, leaner equivalence ratios $0.7 < \phi < 0.9$ correspond to a maximum in NO emissions for premixed flames, with studies reporting emissions in excess of 4500 ppmv [9,10,12,14,16]. However, very lean conditions ($\phi \lesssim 0.6$) can also result in low NO emissions [10,17–19], although increasing amounts of other pollutants such as N_2O and unburnt NH_3 may become an issue [11,18,20,21].

One possibility to stabilize flames with low heating value fuels is to use matrix stabilized combustion in porous media burners (PMBs). Over the past three decades, numerous studies have shown that these burners are a suitable technology for the combustion of conventional hydrocarbon fuels in applications such as industrial burners and gas turbines [22–26]. Of particular interest is the suitability of PMBs for NH_3 utilization in furnaces and industrial burners, which has not received significant attention [6].

Porous media burners consist of open-cell, highly porous, thermally conductive ceramic foams inside of which combustion is performed. Heat recirculation from the combustion products towards the fresh gas by conduction and radiation within the solid ceramic matrix preheats the unburnt gases, enhances flame speed, and improves flame stabilization, thereby extending the flammability limits to mixtures that are otherwise too lean or too rich for combustion in a conventional burner design [23,25]. In a well-designed burner, excess-enthalpy combustion (also known as super-adiabatic combustion) can be achieved. Specifically, by recirculating heat across the flame, the maximum flame temperature can exceed the adiabatic flame temperature of the reactant mixture. The relationship between super-adiabaticity and flame consumption speed is highly non-linear [7,18], and thus even a moderate increase in excess enthalpy can lead to a significantly higher flame speed and a notable improvement in flame stabilization [25,27,28]. In addition to heat recirculation, flame corrugation and other pore-level effects can further enhance the volumetric fuel consumption rates [29,30]. Experimental and numerical studies of these stabilization mechanisms have been reported, including applications to very lean flames over a wide range of flow rates, fuel compositions, operating pressures, and fuel types [26,31,32]. Recent progress in ceramic additive manufacturing also offers interesting perspectives for the development of novel, application-tailored PMB foam topologies [33–35].

The stabilization of NH_3 flames presents similar challenges to that of low–heating-value syngas and very lean hydrocarbon mixtures: a low flame speed with a large flame thickness and a long ignition delay. For very lean conditions and for rich conditions, which have been found to be suitable for low NO operation, these issues are exacerbated [4–6]. Given the non-linear increase of the laminar flame speed of $NH_3/H_2/air$ flames with preheating [7,18], using heat recirculation and super-adiabatic combustion in a PMB is an attractive concept for overcoming these combustion challenges and stabilizing $NH_3/H_2/air$ flames. Three experimental studies have presented proof-of-concepts of these benefits: Rocha et al. [36] used an interface stabilized alumina-zirconia PMB with which they characterized the effect of fuel composition on pollutant emissions and ceramic foam temperature distribution. They studied $NH_3/H_2/air$ and $NH_3/CH_4/air$ flames operated at $\phi = 0.8$, varying the volume fraction of NH_3 in the fuel, and used their experimental measurements to evaluate different chemical mechanisms for NH_3 combustion. Nozari et al. [37] performed a more systematic study on $NH_3/H_2/air$ flame stabilization in a silicon carbide (SiC) PMB at stoichiometric and rich conditions with estimates of combustion efficiency and NO pollutant measurements.

Although this study provided a compelling argument in favor of $NH_3/H_2/air$ combustion inside of SiC PMBs, their results suggest that the flames were not fully stabilized within the porous ceramic foam and instead extended into the exhaust tube. This in turn suggests that the heat recirculation potential of the burner was not fully utilized. In a recent study focusing on lean conditions that had not been extensively considered previously, we demonstrated that a two-zone PMBs can stabilize $NH_3/H_2/air$ flames and that low pollutant emissions can be achieved when the burner is operated near its lean extinction limit [18].

These three studies demonstrate the benefits of matrix stabilized combustion for $NH_3/H_2/air$ mixtures, but more systematic characterizations of flame stabilization properties and pollutant emissions, in conjunction with computational analysis, are required to optimize these burners and to increase their technology readiness level. Therefore, the present study has four main goals: (1) experimentally examine the stability range of PMBs for varying ranges of $NH_3/H_2/air$ mixtures, extending previous works by including pure NH_3/air flames; (2) provide reference data on flame stabilization and pollutant emission for conditions spanning $70\% < X_{NH_3} < 100\%$ and $0.6 < \phi < 1.4$, which extends previous studies to the rich combustion regime; (3) develop and employ reduced-order models to analyze trends in pollutant emissions for $NH_3/H_2/air$ flames in PMBs; and (4) assess the limitations of such low-order models for predicting premixed $NH_3/H_2/air$ combustion in PMBs. The experimental and numerical methods used in this study are described in Section 2. The results are then presented in Section 3, specifically focusing on characterizing effects of operating parameters on flame stability and demonstrating, for the first time, that pure NH_3 flames can be stabilized in PMBs. We then examine pollutant emissions and use numerical simulations to explain the effect of equivalence ratio on the chemical pathways leading to pollutant formation. Finally, we report our main conclusions in Section 4.

2. Methods

2.1. Experimental setup

The burner is shown schematically in Fig. 1. The porous ceramic matrix is constructed by assembling several cylindrical blocks with a diameter of 50.8 mm: along the streamwise direction, two 25.4 mm-thick blocks of 40 pores per inch (PPI) open-cell yttria-stabilized zirconia-alumina (YZA) foam (Selee, Hendersonville, NC, USA); two 25.4 mm-thick silicon carbide (SiC) foam blocks, the first having a large pore size (3 PPI), the second a slightly smaller one (10 PPI), both manufactured by Ultramet (Pacoima, CA, USA). This is an interface-stabilized burner design, where the flame is stabilized at the boundary between the 40 PPI YZA foam, which is designed to quench the flame, and the 3 PPI SiC foam [38]. In order to minimize heat losses from the outer boundary of the burner, the foams are wrapped in high-temperature ceramic paper (Fiberfrax 550, Unifrax, Tonawanda, NY, USA) and placed within a quartz tube at the bottom of which stainless steel balls are used to homogenize the flow. This assembly is attached to an aluminum base. Compared to our previous design, which consisted of only two foam blocks [18], we have increased the burner's length for longer residence time, we have thickened the thermal insulation to reduce radial heat losses, and we have increased the pore size of the SiC foam in the main section of the burner to improve flame stability at very lean and rich conditions by increasing the quenching margin. With these modifications, the cell size of the ceramic foam becomes comparable to the large thermal thickness of NH_3/air flames [18,38].

Table 1 details the characteristics of these ceramic foams. The geometric properties are determined using a 3D reconstruction
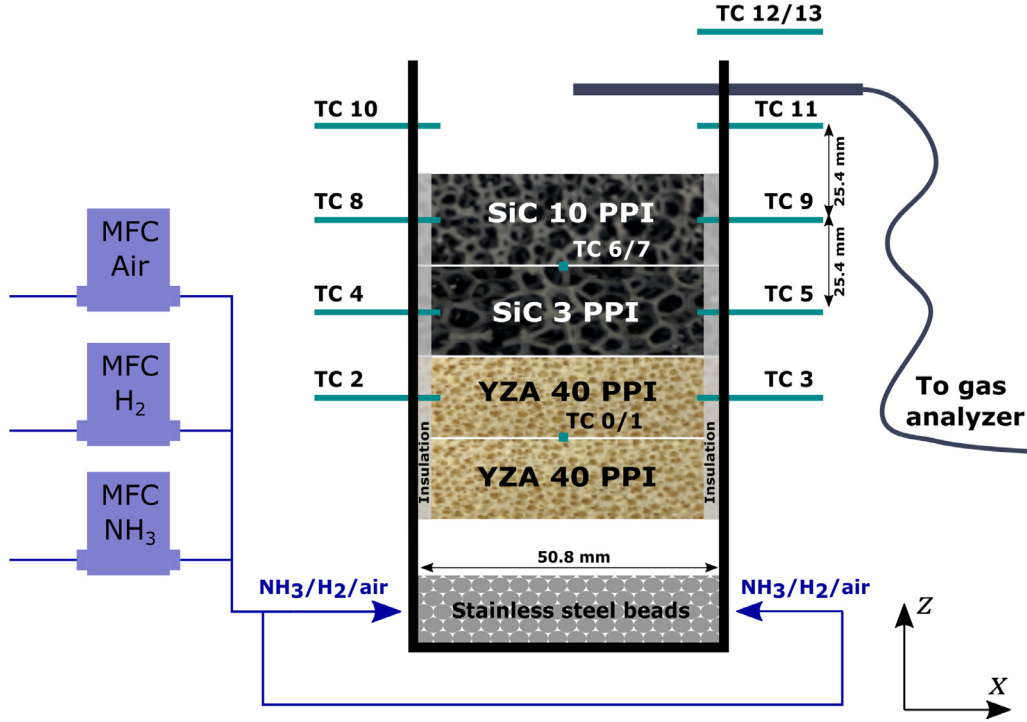
(a)
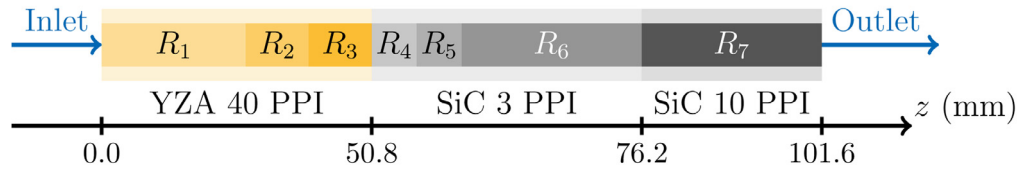
(b)

Fig. 1. (a) Schematic of the experimental apparatus (not to scale). MFC: mass flow controller; SiC: silicon carbide; YZA: yttria-stabilized zirconia alumina; TC: thermocouple. (b) Schematic representation of the reactor network model. R_α indexes the reactors. The reactor lengths are not to scale, the reader is referred to Section 2.3 for more details.

Table 1

Geometric and thermal characteristics of the porous foams employed in the present work. †: values obtained using X-ray μ-XCT; ⋆: information provided by manufacturer.

Description (units)	YZA	SiC	SiC
Pore density (PPI)	40	3	10
Thickness (mm)	2×25.4	25.4	25.4
Porosity ε (%)	82†	84†	84†
Pore diameter d_p (mm)	1.11†	1.56†	1.07†
Cell size d_c (mm)	2.0†	3.2†	2.6†
Specific surface S_v (m^{-1})	2373⋆	246⋆	978⋆
Emissivity ϵ	0.85	0.85	0.85
Effective density ρ_s (g cm^{-3})	4.32†	2.62†	2.62†

of each foam geometry individually obtained with a Zeiss Xradia Versa 520 X-ray micro-computed tomography (μ-XCT) scanner, operated at an X-ray tube voltage/current of 60 kV$_p$/83 mA for SiC, 140 kV$_p$/71 mA for YZA and a total of 2026 projections to resolve the 3D structure. The 3D reconstructed fields are first smoothed with a 3D Gaussian filter with variance of 2 voxels, and segmented between gas, solid, and internal voxels based on density (thresholding using the adaptive method by Otsu [34,39]) and connectivity. The resolved porosity corresponds to the ratio of gas voxels to total voxels. Pore and cell diameters are estimated using a 3D

distance transform watershed algorithm followed by a particle analyzer [40,41].

Experiments are conducted at atmospheric pressure and the reactants are initially at ambient temperature. The flow of all reactants is controlled by an array of mass flow controllers (Alicat, Tucson, AZ, USA, relative accuracy better than 0.8% for present conditions). Chemically pure NH$_3$ and H$_2$ (purity better than 99.995%, Linde, Danbury, CT, USA) are used in this study. The uncertainties on equivalence ratios ϕ and mass fluxes $\dot{m}''$ are thus 1.6% and 0.8%, respectively.

2.2. Instrumentation and measurements

Gas analysis is performed immediately upstream of the exhaust of the quartz tube. Gas samples are quenched and dried before measurements. NO and O$_2$ concentrations are measured using electro-chemical cells (Bridge Analyzers, Bedford Heights, OH, USA). An Emerson Rosemount Analytical thermal conductivity sensor (Shapokee, MN, USA) is used to measure residual H$_2$ in the exhaust stream when operating at fuel-rich conditions. This instrument has a lower detection limit of 0.5% H$_2$, which is too high for measurements at lean conditions. Every instrument is calibrated twice daily with standard gases (pure N$_2$, H$_2$ in N$_2$, and NO in Ar from Linde, Danbury, CT, USA) to compensate for drift. NH$_3$ concentrations are measured using gas measurement tubes from

Gastec (Kanagawa, Japan). All measurements are reported dry and normalized to 15% O_2 concentration following standard practices for gas turbines [42]:

$$X_{i,15\%O_2,dry} = T_{i,dry} \frac{X_{O_2,air} - X_{O_2,ref}}{X_{O_2,air} - X_{O_2,dry,\ sample}},$$

with $X_{O_2,air} = 20.9\%, X_{O_2,ref} = 15.0\%$ (1)

The manufacturer's specified measurement uncertainty for the NO, NH_3, H_2 and O_2 cells are, respectively, 5%, 10%, 3% and 5%. During our twice daily calibrations, we noted a higher than specified measurement drift for the NO cell and therefore used a larger uncertainty of 11% for these results. All measurements were averaged for at least 2 min after stabilization, leading to a statistical uncertainty better than 4% for the worst case condition reported in the present work. At operating conditions corresponding to extrema in pollutant emissions, measurements were repeated at least 3 times to verify the absence of long term drift. With this, we consider that the relative uncertainties for the normalized NO and NH_3 emission measurements are 20%, while for unburnt H_2, which is not normalized, relative measurement uncertainties are estimated to be 7%. In addition to exhaust gas measurements, nicrotherm-sheathed type-N thermocouples (TC Direct, Hillside, IL, USA) are used to assess flame stability by monitoring exhaust gas and ceramic foam temperatures over time. A NI-9213 thermocouple module within a NI cDAQ-9189 chassis is used to read the measurements. Measurement biases introduced by our thermocouple setup are corrected analytically using the method presented in Appendix A.

The experimental procedure used to determine flame stability is as follows: after reaching a specific operating condition, we wait for thermal stabilization, which is characterized by a maximum change of 10 K over two minutes on all thermocouples installed in the burner; if thermal stabilization can be reached while maintaining combustion within the open-cell ceramic foam, then the operating condition is considered stable. Otherwise, the condition is categorized either as extinction or as flashback, if the flame propagates upstream to $z \leq 50.8$ mm.

2.3. Reactor network model

To provide further analysis on pollutant formation and to study the effect of heat recirculation within the ceramic matrix, we extend the network model proposed by Mohaddes et al. [25] to include a detailed description of NH_3/H_2/air chemistry. The low order model consists of $N_r = 7$ homogeneous continuously stirred reactors, designated R_α, with $\alpha = 1, \dots, N_r$, see Fig. 1. The first three reactors R_1, R_2, R_3 (with respective lengths 38.1 mm, 6.35 mm and 6.35 mm) represent the YZA foam section of the burner, the next three reactors R_4, R_5, R_6 (lengths 3.12 mm, 3.12 mm and 19.1 mm) represent the 3 PPI SiC foam and the last reactor R_7 with a length of 25.4 mm represents the 10 PPI SiC. This configuration was found to best reproduce pollutant emissions in the burner with a minimal number of reactors, and adequately models heat recirculation and excess-enthalpy combustion within the burner.

The reactor network is implemented using the extensible reactor network framework of Cantera [43]. The source code for this model is attached as supplementary materials. The gas phase thermo-chemical and transport properties are computed based on the 29 species, 203 reactions mechanism by Stagni et al. [44], which has been validated against experimental measurements conducted at ambient pressure, over a wide range of operating conditions, extending from lean to rich and from hydrogen assisted to pure ammonia [45,46]. A system of $N_r(2 + N_s)$ ordinary differential equations is solved, where N_s is the number of species in the chemical mechanism, with two additional equations for the gas-

and solid-phase temperatures. Because steady-state combustion is considered, the mass flux is prescribed. Each reactor, indexed with subscript α, is modeled by solving the following governing equations for N_s species mass fractions Y_i, the gaseous and solid temperatures, T_g and T_s, respectively:

$$\rho_{g,\alpha} \frac{dY_{i,\alpha}}{dt} = \dot{\omega}_{i,\alpha} + \frac{\dot{m}'' A_{CS}}{V_\alpha \varepsilon_\alpha} (Y_{i,\alpha-1} - Y_{i,\alpha}),$$ (2a)

$$\rho_{g,\alpha} c_{p,g,\alpha} \frac{dT_{g,\alpha}}{dt} = \frac{\dot{m}'' A_{CS}}{V_\alpha \varepsilon_\alpha} \left(h_{\alpha-1} - \sum_{i=1}^{N_s} h_{i,\alpha} Y_{i,\alpha-1} \right)$$
$$+ \dot{q}_{chem,\alpha} - \frac{h_{v,\alpha}(T_{g,\alpha} - T_{s,\alpha})}{\varepsilon_\alpha},$$ (2b)

$$(1 - \varepsilon_\alpha)\rho_{s,\alpha} c_{s,\alpha} \frac{dT_{s,\alpha}}{dt} = h_{v,\alpha}(T_{g,\alpha} - T_{s,\alpha}) + \frac{\dot{q}_{loss,\alpha}}{V_\alpha} + \frac{\dot{q}_{ax,\alpha}}{V_\alpha},$$ (2c)

where the subscripts g, and s, respectively, designate the gaseous and solid phases. $\rho_{g,\alpha}$ is the density in reactor R_α with volume V_α and porosity ε_α; and $\dot{\omega}_{i,\alpha}$ is the net production rate of species i. A_{CS} is the cross-sectional area of the burner. For the conservation of energy in the gas phase (Eq. (2b)), $c_{p,g}$ is the isobaric heat capacity of the gas phase, $\dot{q}_{chem}$ is the heat release rate due to chemical reactions, h is the specific enthalpy, and h_v is the volumetric heat transfer coefficient between the solid phase and gas phase. In Eq. (2c), the radiative heat loss $\dot{q}_{loss,\alpha}$ is given by

$$\dot{q}_{loss,\alpha} = -\sigma\epsilon \left(T_{s,\alpha}^4 - T_{amb}^4 \right) (\tau \pi D L_\alpha + A_{CS} \delta_{\alpha,N_r}).$$ (3)

This includes both contributions of radial heat losses on the outer side of the foam and of the end of the burner. σ is the Stefan–Boltzmann constant, $\tau = 0.5$ is the estimated optical transmissivity of the insulation layer, D is the burner diameter, L_α is the length of reactor R_α, δ_{α,N_r} is the Kronecker delta, and $T_{amb} = 300$ K is the ambient temperature. Heat transfer between neighboring reactors $\dot{q}_{ax,\alpha}$ is modeled by

$$\dot{q}_{ax,\alpha} = 2A_{CS}\left(\lambda_{s,eff,\alpha} + \lambda_{rad,\alpha}\right) \left(\frac{T_{s,\alpha-1} - T_{s,\alpha}}{L_{\alpha-1} + L_\alpha} + \frac{T_{s,\alpha+1} - T_{s,\alpha}}{L_{\alpha+1} + L_\alpha} \right),$$ (4)

which accounts for both solid heat conduction, and solid radiative heat transfer between neighboring reactors. The effective solid phase heat conductivity, was computed in previous work [26]. The temperature dependency is given by a correlation derived from experimental data by Nilsson et al. [47] and Slack [48]:

$$\lambda_{s,eff} = \begin{cases} 0.3 \ (\text{Wm}^{-1} \ \text{K}^{-1}) & \text{for YZA;} \\ 1857(1 - \varepsilon)T_s^{-0.5332} \ (\text{Wm}^{-1} \ \text{K}^{-1}) & \text{for SiC;} \end{cases}$$ (5)

with T_s expressed in K. Similarly, the solid phase heat capacity is given as [49]:

$$c_s = \begin{cases} 910 - 2.40 \times 10^5 T_s^{-1.15} \ (\text{J kg}^{-1} \ \text{K}^{-1}) & \text{for YZA;} \\ 1522 - 9.02 \times 10^4 T_s^{-0.82} \ (\text{J kg}^{-1} \ \text{K}^{-1}) & \text{for SiC.} \end{cases}$$ (6)

The volumetric heat transfer coefficient is computed as:

$$h_v = \frac{S_v \lambda_g}{d_h} Nu.$$ (7)

using the Nusselt number correlation proposed by Bedoya et al. [29]:

$$Nu = 3.7Re^{0.38}Pr^{0.25}, \ \text{with } Re = \frac{\rho_g u d_h}{\mu_g}, \ \text{and } Pr = \frac{c_{p,g}\mu_g}{\lambda_g},$$ (8)

with $u = \dot{m}''/(\rho_g \varepsilon)$ the interstitial gas velocity and μ_g the gas phase viscosity. The radiative heat conductivity is computed with the Rosseland model [50]:

$$\lambda_{\mathrm{rad}} = \frac{16\sigma T_s^3}{3\kappa}, \tag{9}$$

with extinction coefficient $\kappa = (3/d_p)(1 - \varepsilon)$ [51].

3. Results

3.1. Flame stabilization

The primary advantage of porous media burners is their ability to enhance the stabilization of flames with poor combustion properties [22–25]. In this section we investigate the stability limits of our PMB as a function of three operating parameters: the mass flux of reactants through the burner $\dot{m}''$, the equivalence ratio ϕ, and the volumetric ratio of H_2 to NH_3 in the fuel (expressed as the volume fractions X_{NH_3} and X_{H_2} in the fuel such that $X_{H_2} + X_{NH_3} = 100\%$). We follow the experimental procedure outlined in Section 2.2 and the results of this systematic investigation are shown in Fig. 2. Regions that have been greyed out in Fig. 2 could not be investigated because of either safety or mass flow controller limitations.

Figure 2 (a) shows that stable combustion can be achieved with pure NH_3 in this burner. This is, to the best of our knowledge, the first demonstration of PMB stabilizing a pure NH_3 flame, and is most likely the result of using a larger pore size and better thermal insulation than in previous studies [18,37]. Stable combustion is achieved for mixture compositions between $0.75 \leq \phi \leq 1.4$. This corresponds to the region of sufficiently high laminar burning velocity and sufficiently thin thermal flame thickness to support NH_3/air flame stabilization [7,18].

Figure 2 (b) shows the stability diagram for the same burner operated with a fuel mixture of $X_{NH_3} = 85\%$. At this condition, the maximum mass flux through the burner is increased by 75% compared to the pure NH_3 case and the lean extinction limit decreases to $\phi_{\mathrm{ext}} = 0.65$. Increasing the H_2 content further, with $X_{NH_3} = 70\%$, yields further improvement of burner stability, with lean extinction limits as low as $\phi_{\mathrm{ext}} = 0.55$ being achieved. Figure 2(c) also shows that the burner is able to stabilize flames at mass fluxes of $\dot{m}'' = 1.5$ kg m^{-2} s^{-1}, corresponding to a twofold increase compared to $X_{NH_3} = 85\%$. Flashback occurs at low mass flux ($0.2 \leq$

$\dot{m}'' \leq 0.3$ kg m^{-2} s^{-1}), and stoichiometric and slightly rich conditions ($0.95 \leq \phi \leq 1.2$). At these conditions, the flame is no longer quenched in the YZA foam and slowly propagates upstream. Flashback in porous media and micro-combustion is a complex coupled phenomenon that is currently not well understood. A detailed experimental and theoretical analysis on the flame propagation speed in a meso-scale tubular micro-reactor with heat loss, can be found in Ju and Xu [52]. In this study, the authors found that higher laminar flame speeds lead to higher flame propagation speeds. This explains the occurrence of flashback at $0.95 \leq \phi \leq 1.2$ observed in our PMB, as this range of equivalence ratio corresponds to a region of relatively high laminar speeds for NH_3/H_2/air flames [7,18]. However, at low flow rates, Ju and Xu [52] noted the existence of a bifurcation due to the non-linear coupling between the flame and the temperature field of the solid. At a fixed equivalence ratio, the flame propagation speed has a local maximum at a critical flow rate $\dot{m}''_{\mathrm{crit}}$ and decreases if the flow rate is reduced below $\dot{m}''_{\mathrm{crit}}$. This bifurcation might explain the isolated flashback region observed in Fig. 2(c), where stable combustion is observed at the lowest flow rate $\dot{m}'' = 0.1$ kg m^{-2} s^{-1}.

The turndown ratio of a burner is defined as the ratio between the highest and lowest mass flux at which stable combustion can be achieved. A high turndown ratio is particularly desirable for industrial applications. At $X_{NH_3} = 70\%$, we successfully demonstrate a turndown ratio better than 15:1. This is comparable and exceeds state-of-the-art hydrocarbon-fuel-based industrial burners with reported turndown ratios of 1:10 to 1:15 in premixed operation [53]. Note that our NH_3 gas delivery system does not allow to perform experiments at mass fluxes higher than 1.5 kg m^{-2} s^{-1} or lower than 0.1 kg m^{-2} s^{-1}, so that the reported results are a conservative estimate of the potential of NH_3 PMBs for high turndown ratios.

Volumetric thermal power density is defined as the ratio of the thermal power of the combustor to the volume of the combustion region. High power density results in reduced weight, cost, and improved efficiency in many space-constrained devices such as jet engines, gas turbines and furnaces, and is another advantage of porous media combustion. For the purpose of the present work, we compute the power density by considering an ideal combustion efficiency, and we only consider the volume of the combustion region itself in our calculations. For the PMB, we use the volume of the SiC foams independently of whether their entire volume is utilized or not during the combustion process. In this respect the reported volumetric power densities for the PMB are more
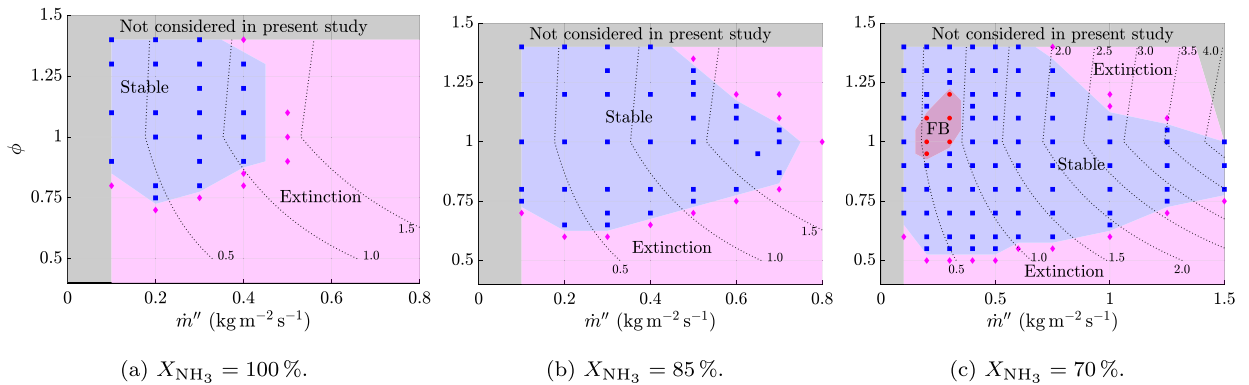

(a) $X_{NH_3} = 100\%$.   (b) $X_{NH_3} = 85\%$.   (c) $X_{NH_3} = 70\%$.

Fig. 2. Burner stability map, shown as a function of the fuel composition, equivalence ratio ϕ, and mass flux $\dot{m}''$. Each point in the map corresponds to one experiment. The blue region (squares) indicates conditions at which the burner is stable, the red region (circles) indicates the occurrence of flashback and the magenta region (diamonds) corresponds to conditions where no flame could be stabilized. $X_{H_2} + X_{NH_3} = 100\%$. The dotted lines are iso-contours of thermal power per unit surface $\mathcal{P}'' = \dot{m}''(h_{\mathrm{fresh}} - h_{\mathrm{eq.}})$, where we assume chemical conversion to equilibrium, with h_{fresh} (resp. h_{eq}) the mass enthalpy of the fresh reactants (resp. products at chemical equilibrium). $\mathcal{P}''$ is indicated in MWm^{-2}. (For interpretation of the references to colour in this figure legend, the reader is referred to the web version of this article.)

conservative than our estimates for swirl-stabilized flames. Using experimental investigations published in the literature, we estimated the volume of swirl flames based on chemiluminescence images. The highest thermal power density demonstrated in this PMB is 62 MW m^{-3}. This is substantially higher than swirl-stabilized NH_3 flames with comparable exergy, at stoichiometry, and operating under atmospheric pressure. From published experimental studies we estimate that the typical power densities for these swirled NH_3 flames are on the order of 5 to 22 MW m^{-3} [16,54,55].

3.2. Pollutant emissions

We now focus on pollutant emissions. Table 2 summarizes the operating conditions for which each type of gas analysis measurement has been performed. Figure 3 shows the measured NO and unburnt NH_3 emissions of the PMB, normalized to 15% O_2, when operated at two mass fluxes $\dot{m}'' = 0.3$ and 0.4 kg m^{-2} s^{-1}, and three volumetric NH_3 fuel fractions: $X_{NH_3} = \{70\%, 85\%, 100\%\}$. Following a similar trend to swirled NH_3 combustion [4–6,56], high NO production is observed for flames close to stoichiometric conditions, with a maximum reached around $\phi \approx 0.8$–0.9. A 33% increase in mass flux from 0.3 to $\dot{m}'' = 0.4$ kg m^{-2} s^{-1} yields an increase in NO emissions by 60% when operating at near stoichiometric conditions. Low NO emissions are achieved for rich conditions ($\phi \geq 1.2$) and very lean conditions, near the burner's ex-

Table 2

Summary of operating conditions for which pollutant measurements are performed, and for which numerical simulations with the reactor network model (RNM) are conducted. LDL: measurement are performed but the concentration is below the lower detection limit of the sensor.

X_{NH_3}	$\dot{m}''$ (kg m^{-2} s^{-1})	ϕ	Experiments			RNM
			NO	NH_3	H_2	
100	0.3	0.85–1.0	yes	yes	LDL	yes
		1.1–1.3	yes	yes	yes	yes
	0.4	0.9–1.1	yes	yes	no	yes
85	0.3	0.65–1.0	yes	yes	LDL	yes
		1.1–1.4	yes	yes	yes	yes
	0.4	0.68–1.4	yes	yes	no	yes
70	0.3	0.53–1.0	yes	yes	LDL	yes
		1.1–1.4	yes	yes	yes	yes
	0.4	0.53–1.4	yes	yes	no	yes
		0.2–0.5	1.3	yes	yes	yes	no
		0.7–1.5		yes	no	yes	no
55	0.3	0.45–0.7	yes	yes	LDL	no

tinction limit ($\phi \leq 0.6$). At lean operating conditions, unburnt NH_3 emissions are generally at or below the lower detection limit of our measurement apparatus. As one approaches the lean extinction limit, unburnt NH_3 emissions quickly increase due to poorer flame stabilization and can reach up to 2% (normalized to 15% O_2). High unburnt NH_3 emissions are also observed at $\dot{m}'' = 0.4$ kg m^{-2} s^{-1}

(a) NO, $\dot{m}'' = 0.3 \, \text{kg} \, m^{-2} \, s^{-1}$.

(b) NH_3, $\dot{m}'' = 0.3 \, \text{kg} \, m^{-2} \, s^{-1}$.

(c) NO, $\dot{m}'' = 0.4 \, \text{kg} \, m^{-2} \, s^{-1}$.

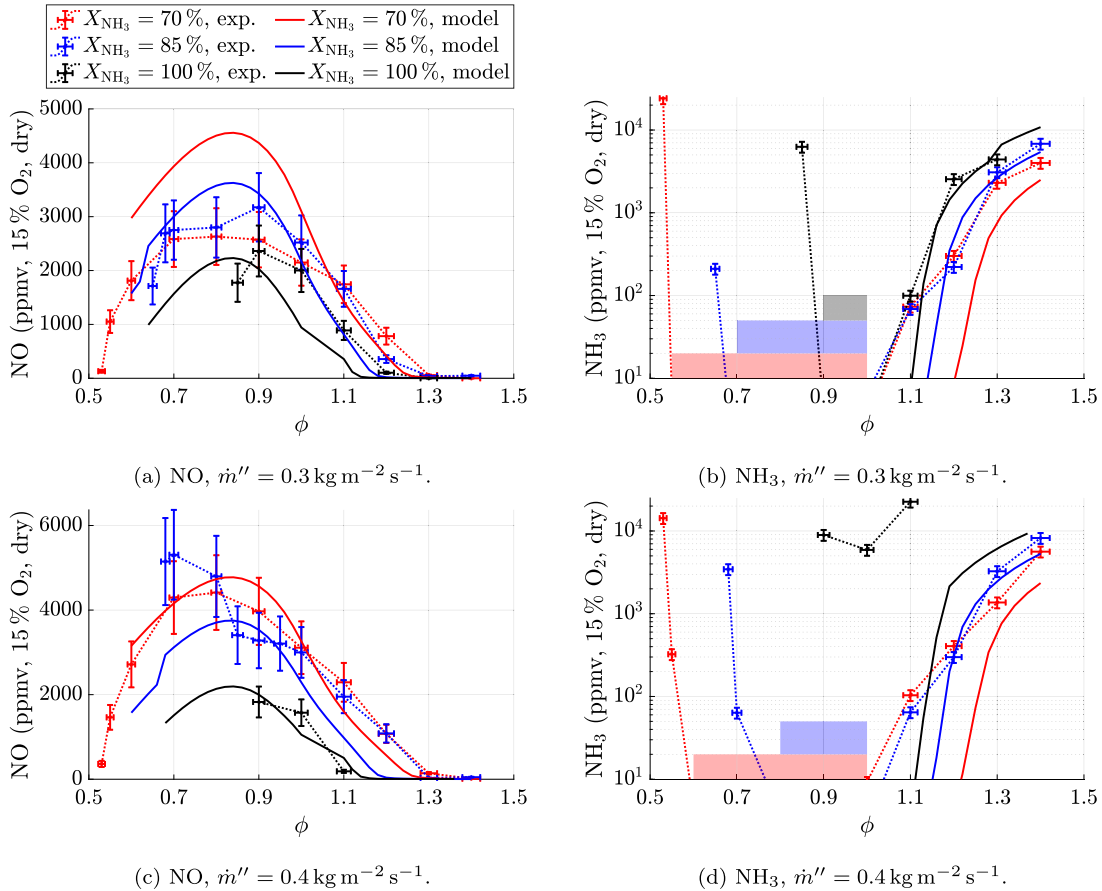(d) NH_3, $\dot{m}'' = 0.4 \, \text{kg} \, m^{-2} \, s^{-1}$.

Fig. 3. NO and unburnt NH_3 emissions of the burner, measured dry and cold and normalized to 15% O_2 following [42], shown as a function of X_{NH_3} and equivalence ratio ϕ, for two mass fluxes (a,b) $\dot{m}'' = 0.3$ kg m^{-2} s^{-1} and (c,d) 0.4 kg m^{-2} s^{-1}. For unburnt NH_3, the colored shaded regions correspond to conditions at which unburnt NH_3 concentrations were below the lower detection limit of the measurement system. Markers and dotted lines are used for experimental data, while continuous lines represent the output of the reactor network model introduced in Section 2.3.
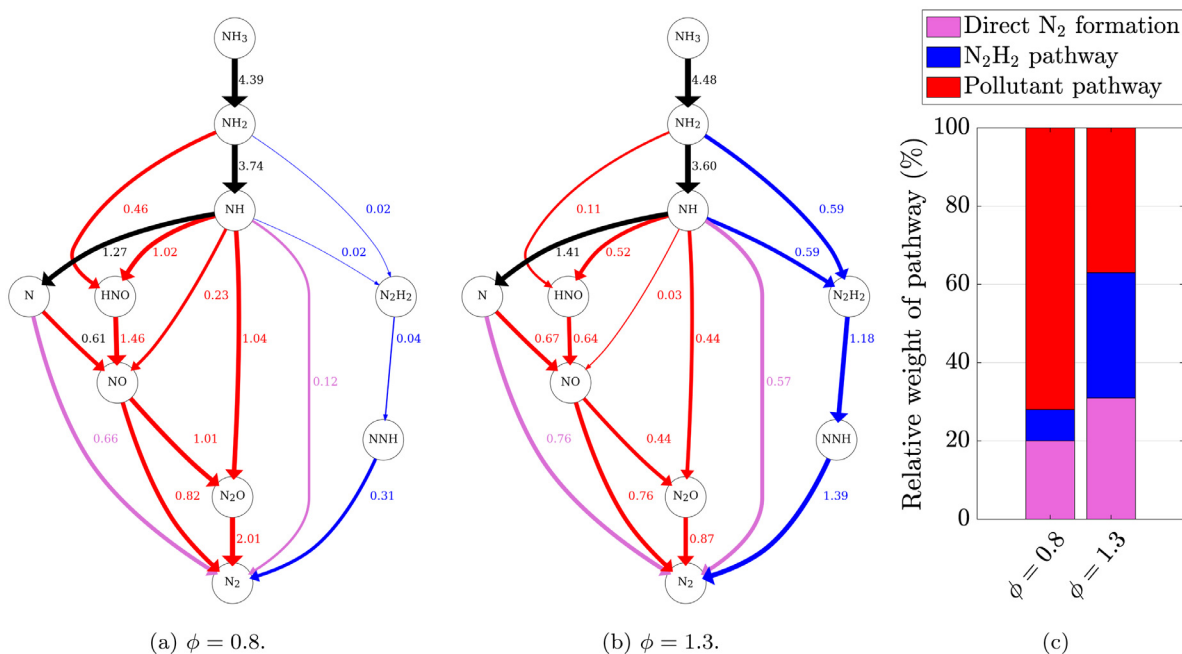
Fig. 4. Reaction pathway diagrams following the elemental flux of N in reactor R_4 ($z = 50.8$ mm), the location where the flame stabilizes. The analysis is performed for two conditions: (a) $\phi = 0.8$, and (b) $\phi = 1.3$, with $X_{NH_3} = 70\%$ and $\dot{m}'' = 0.3$ kg m^{-2} s^{-1}. The elemental fluxes of N in kmol$_N$ m^{-3} s^{-1} are normalized by the molar fraction of the inlet mixture, calculated including both fuel and oxidizer. The numbers on the arrows indicate the magnitude of the molar elemental flux between species. The width of the arrow is scaled logarithmically by this magnitude. Some minor elementary reaction pathways with very low elemental fluxes, such as $NH_2 + NO = N_2 + H_2O$ and $NH_2 + NO = NNH + OH$, which both account for less than 2.5% of the N elemental flux, have been removed to improve readability. (c): relative weight of each of the major chemical pathways.

and $X_{NH_3} = 100\%$, which again can be attributed to poor flame stabilization as these conditions are found near the upper blow-off limit of the burner, see Fig. 2(a). N_2O is another significant pollutant associated with NH_3 combustion. Although we are not able to report experimental measurements for this pollutant, we discuss these emissions in Fig. S1 of the supplemental materials using our numerical model.

Comparing the results of the reactor network model (continuous lines) with experimental measurements (symbols and dotted lines) in Fig. 3 shows overall good qualitative agreement for NO and NH_3 emissions obtained over a wide range of operating conditions. However, the reactor network model is unable to accurately predict lean extinction, blow-off (near $\dot{m}'' = 0.4$ kg m^{-2} s^{-1} and $X_{NH_3} = 100\%$) and the increase in unburnt NH_3 emission that occurs as one nears the extinction limit. In these operating regions, multidimensional effects such as flame front corrugation, stretch, and local extinction are present, leading to a decrease in combustion efficiency and ceramic foam temperature [30,57,58]. The reactor network model is unable to capture such effects. Nevertheless, good agreement is obtained at stoichiometric and rich operating conditions, which allows to study pollutant formation in these regions using pathway analysis.

The results from the model show that NO is mainly formed in the hot flame region, located near the interface between the YZA and SiC porous ceramic foams, see supplementary materials, Figs. S3 and S4. The magnitude of the formation rate depends on the equivalence ratio and is highest at $\phi = 0.80$. Downstream of the flame region, NO is slowly consumed. At rich conditions ($\phi \geq 1.2$), the formation rate in the flame region and the consumption rate in the post-flame region are of similar orders of magnitude, leading to fairly low NO emissions. On the contrary, at near stoichiometric conditions ($0.8 \leq \phi \leq 1.1$), the consumption rates of NO and NO_2 in the post-flame region are up to two orders of magnitude lower than their formation rates in the flame region.

To understand the chemistry of the flame region, associated with high NO formation rates in this burner, we show in Fig. 4 reaction pathway diagrams in this region at two representative equivalence ratios: $\phi = 0.80$ and $\phi = 1.30$. In these diagrams, we follow the elemental fluxes of N. To facilitate a direct comparison between the two cases, all fluxes are normalized by the respective molar fraction of NH_3 in the premixed inlet flow containing both fuel and oxidizer. Following N atoms originally present in the fuels and forming N_2, one may distinguish three main pathways:

1. direct N_2 formation, shown in magenta in Fig. 4;
2. the N_2H_2 pathway, involving N_2H_2 and NNH as intermediates, illustrated in blue in Fig. 4;
3. the pollutant pathway, involving NO and N_2O as intermediates, illustrated in red in Fig. 4.

The relative weight of each of these pathways is shown for both cases in Fig. 4(c). At $\phi = 0.80$ (Fig. 4(a)), the relative weight of the pollutant pathway (red) is quite high: 72% of N atoms being converted from NH_3 to N_2 go through this pathway. NO and N_2O are thus significant intermediate species in the combustion process of NH_3 at this condition. This is in direct contrast with operating at rich conditions (Fig. 4(b)), where we find that the pollutant pathway (red) only accounts for 37% of the N elemental flux in the global reaction $NH_3 +$ reactants $\rightarrow N_2 +$ products. N_2H_2 (blue pathway) is mainly formed through the reaction of NH with NH_2, so that its formation rate increases at rich conditions. The relative weight of the N_2H_2 pathway is therefore increased from 8% to 32% when increasing ϕ from 0.8 to 1.3, while that of the direct N_2 formation remains comparable (20% at $\phi = 0.8$ and 31% at $\phi = 1.3$).

The remainder of the present article will focus on a more detailed analysis of pollutant formation in the two operating regimes found most beneficial for NO emission: rich and very lean combustion. Specifically, we will focus on the effect of secondary

operating parameters (X_{NH_3}, burner temperature, and mass flux $\dot{m}''$) on these pollutant emissions.

3.3. Pollutant formation near the lean limit

Operating the porous media burner at conditions near the lean extinction limit is a practical solution for achieving low NO emissions [16–19], and we examine here pollutant formation in this regime. We focus on a single mass flux of $\dot{m}'' = 0.3$ kg m^{-2} s^{-1}, corresponding to conditions at which very lean operation can be achieved (Fig. 2), and consider H$_2$/NH$_3$ mixtures with $X_{NH_3} = \{55\%, 70\%, 85\%\}$.

Figure 5 shows the composition of the exhaust gas as a function of equivalence ratio. NO emissions are normalized to 15% O$_2$ to compensate for dilution. At $X_{NH_3} = 85\%$, the extinction limit of the burner is not reached at sufficiently lean conditions to achieve low NO operation: emissions are on the order of 1700 ppmv. Using high H$_2$ blending, at $X_{NH_3} = 70\%$ and 55%, lean extinction limits as low as $\phi = 0.53$ and $\phi = 0.45$, respectively, can be achieved. At these conditions, NO emissions range between 10 and 150 ppmv. In contrast, unburnt NH$_3$, which is generally not a significant issue under lean conditions, is measured at concentrations of 100 to 200 ppmv in the very lean region, and up to 20,000 ppmv at the lean limit. We could not detect unburnt H$_2$ at these conditions, in-

dicating that its concentration is lower than the lower detection limit of 0.5% of our thermal conductivity gas analyzer.

3.4. Pollutant formation in fuel-rich conditions

Figure 6 shows measurements of the volumetric exhaust concentration of NO, unburnt NH$_3$ and unburnt H$_2$, for a constant mass flux of $\dot{m}'' = 0.3$ kg m^{-2} s^{-1}, as a function of equivalence ratio ($\phi \geq 1.0$) and volumetric fractions of NH$_3$ in the fuel ($X_{NH_3} = \{70\%, 85\%, 100\%\}$). NO emissions decrease with increasing

(a) NO.

(b) NH$_3$.

(c) H$_2$.
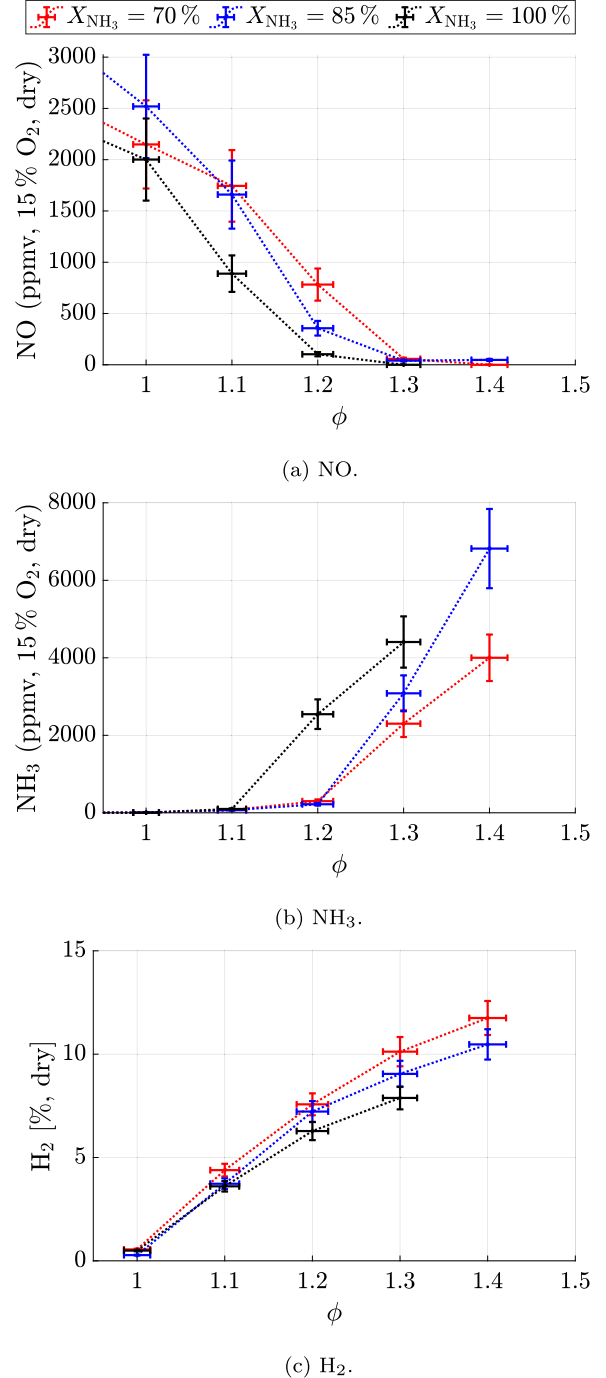
Fig. 6. Measurements of the NO, NH$_3$, and H$_2$ emissions of the burner operating at rich conditions, measured dry and cold. NO and NH$_3$ are reported normalized to 15% O$_2$ following [42]. The mass flux is kept constant at $\dot{m}'' = 0.3$ kg m^{-2} s^{-1}.

(a) NO.

(b) NH$_3$.

Fig. 5. NO and unburnt NH$_3$ emissions of the burner near the lean extinction limit, measured dry and cold and normalized to 15% O$_2$ following [42]. $\dot{m}'' = 0.3$ kg m^{-2} s^{-1}. For unburnt NH$_3$, the colored shaded regions correspond to conditions at which unburnt NH$_3$ concentrations were below the lower detection limit of the measurement system.
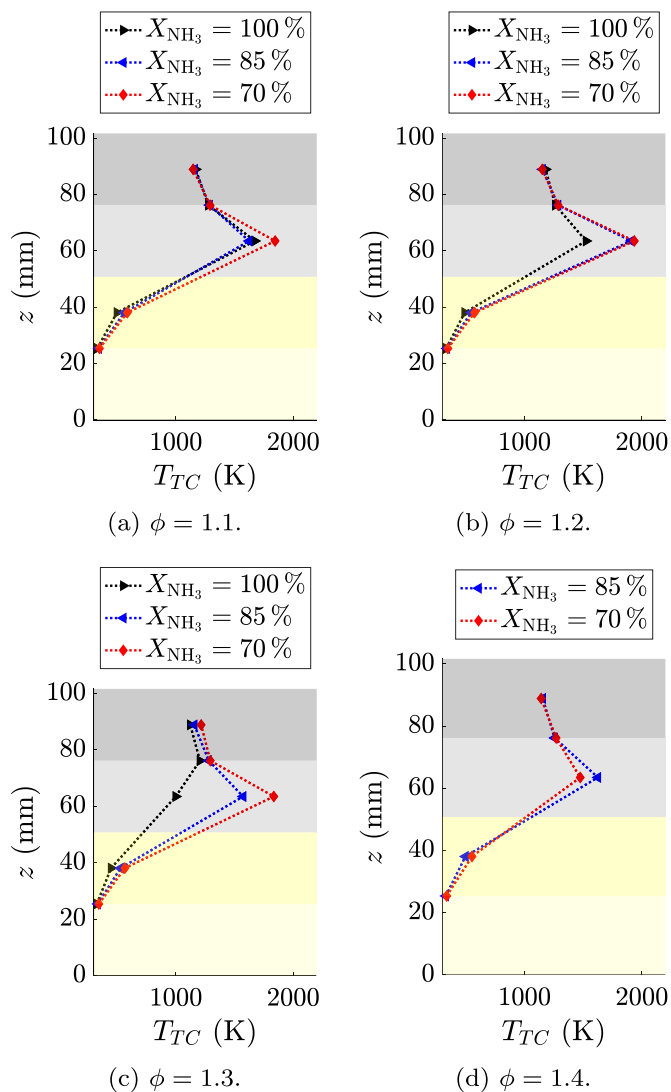
Fig. 7. Effect of operating parameters on thermocouple temperature during fuel-rich operation. The NH_3 volume fraction in the fuel is varied for equivalence ratios: (a) $\phi = 1.1$; (b) $\phi = 1.2$; (c) $\phi = 1.3$; (d) $\phi = 1.4$, and (a–d) $\dot{m}'' = 0.3$ kg m^{-2} s^{-1}.

equivalence ratio. At $\phi \geq 1.3$, NO emissions are on the order of 50 ppmv. Simultaneously, increasing unburnt fuel concentrations are found in the exhaust gases at richer conditions. A large fraction of these unburnt reactants are in the form of unburnt H_2, whose volume fraction in the exhaust gases gradually increases to 12%. For $X_{NH_3} = \{70\%, 85\%\}$ and $\phi \leq 1.2$, only trace amounts of unburnt NH_3 (up to 250 ppmv) are present in the exhaust gases, indicating that almost all NH_3 in the fuel stream is either oxidized or reformed. For $X_{NH_3} = 100\%$, significant amounts of unburnt NH_3 are present in the exhaust stream at $\phi = 1.2$. This is mainly attributed to the lower flame temperature, which is further discussed in the next paragraph.

In Fig. 7(a), thermocouple measurements for $\phi = 1.1$ show that H_2 blending does not significantly impact either the flame anchoring position or the temperature profile. In addition, at $\phi = 1.1$, we note from Fig. 6 that the composition of the unburnt reactants in the exhaust is also relatively insensitive to X_{NH_3}. In contrast, for $\phi = 1.2$ (Fig. 7(b)), the flame with $X_{NH_3} = 100\%$ has a significantly lower peak temperature than its $X_{NH_3} = 85\%$ and $X_{NH_3} = 70\%$ counterparts. This difference in flame topology and burner operating temperature can be attributed to a lower combustion effi-

ciency with higher unburnt fuel in the exhaust stream (Fig. 6), and to an overall poorer flame stabilization. For $\phi = 1.3$ (Fig. 7(c)) and $\phi = 1.4$ (Fig. 7(d)), more unburnt fuel (NH_3 and H_2) is found in the exhaust stream. At $\phi = 1.3$ and $X_{NH_3} = 100\%$, the flame is stabilized within the 10 PPI SiC foam ($z \geq 76.2$ mm), with the 3 PPI SiC foam ($50.8 \leq z \leq 76.2$ mm) acting as an extended preheating region. At $\phi = 1.4$ and $X_{NH_3} = 100\%$, the flame is fully blown off. In general, the ratio of unburnt H_2 to unburnt NH_3 in the burner's exhaust increases as X_{NH_3} is decreased. Three compounding factors explain this trend: (1) the fuel stream contains less NH_3 and more H_2, (2) flames tend to stabilize further downstream, thereby decreasing the residence time, and (3) the burner's operating temperature decreases.

At these rich conditions, we again rely on a reaction pathway analysis with the detailed chemistry reactor network model to analyze our experimental measurements. Similarly to Fig. 4, we focus on the region located around $z = 50.8$ mm, corresponding to the flame location and the region of highest NO formation rate. 1D profiles of temperature, species concentrations, and net formation rate are reported in the supplemental materials, Figs. S5 and S6. We consider the following conditions: $X_{NH_3} = 100\%$ and $X_{NH_3} = 70\%$ for $\dot{m}'' = 0.3$ kg m^{-2} s^{-1} and $\phi = 1.2$, corresponding respectively to one case for which residual NH_3 and low NO are present in the exhaust stream and to another case where almost all NH_3 is either oxidized or reformed and NO emissions are higher. In Fig. 8(a) and (b), we find similar elemental N pathways between these two cases, and generally a similar structure to that identified in Section 3.2. A significant difference, however, is the rate of NH_3 decomposition (NH_3 + reactant $\rightarrow NH_2$ + product), which is here a rate limiting step. The reactions associated with this step have an aggregated 20% higher rate for $X_{NH_3} = 70\%$ compared to $X_{NH_3} = 100\%$. These reactions have a high activation energy [44], and therefore a high sensitivity to the burner's temperature. The higher gas temperature ($T_g = 2241$ K for $X_{NH_3} = 70\%$), compared to $T_g = 2137$ K for $X_{NH_3} = 100\%$, is therefore the main cause of this decrease in consumption rate. It can be seen that there is a significant difference in the relative weight of the NH_3 + reactants $\rightarrow N_2$ + products pathways as a function of X_{NH_3} (Fig. 8(c)): at $X_{NH_3} = 100\%$, 46.5% of N_2 is formed through the N_2H_2 pathway (blue arrows), compared to only 21.9% at $X_{NH_3} = 70\%$. On the contrary, the pollutants (NO and N_2O) pathway (red arrows) accounts for 47.1% of N_2 formation at $X_{NH_3} = 70\%$, but only 30.0% at $X_{NH_3} = 100\%$. A major contributor to this difference in reaction pathways is the higher temperature of the $X_{NH_3} = 70\%$ flame. To conclude this analysis, the lower NO emissions measured experimentally at $X_{NH_3} = 100\%$ can mainly be attributed to two factors: (1) in the flame region, due to a lower gas temperature, the pollutant pathway to N_2 formation is less active than for other conditions and 40.0% less NO is created as a reaction intermediate; (2) compounding on this lower NO formation rate, higher concentrations of unburnt NH_3, and of NH and NH_2 radicals are present in the post-flame region at $X_{NH_3} = 100\%$. This favors the NO reburn pathways, with a 35.4% greater NO consumption rate, thereby further reducing NO emissions.

Mass flux affects heat recirculation, ceramic matrix temperature and flame surface density within the burner. Its effect on burner emissions is therefore both of fundamental and practical interest and is explored in Fig. 9 for $\phi = 1.3$ and $X_{NH_3} = 70\%$. This operating condition is selected because flames can be stabilized over a wide range of mass fluxes, while NO emissions remain relatively low. Higher mass fluxes lead to improved reforming of NH_3: the unburnt NH_3 emissions in the exhaust decreases while the unburnt H_2 volume fraction increases. Extrapolating on the
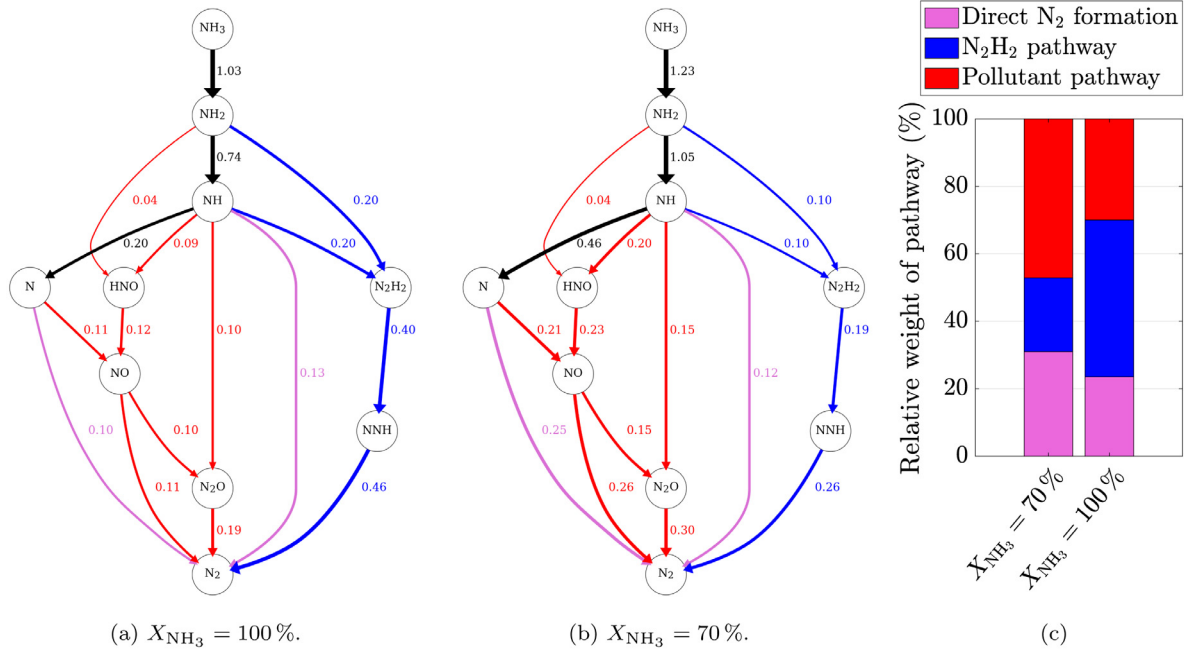
Fig. 8. Reaction pathway diagrams following the elemental flux of N. The analysis is performed at two conditions: (a) $X_{NH_3} = 100\%$ and (b) $X_{NH_3} = 70\%$, at $\dot{m}'' = 0.3$ kg m^{-2} s^{-1} and $\phi = 1.2$. The analysis is performed for reactor R_4 ($z = 50.8$ mm), where most NH$_3$ consumption occurs. To allow for comparison between cases, the elemental fluxes in kmol$_N$ m^{-3} s^{-1} are multiplied by X_{NH_3}. In the present diagram, the width of the arrows is scaled logarithmically to the elemental flux between species, and the magnitude of that flux is indicated by the labels. The reader is referred to Section 3.2 for the interpretation of the color code employed in the present figure. Some minor reaction pathways with low elemental fluxes have been removed to improve readability. (c): Relative weight of each of the major chemical pathways.
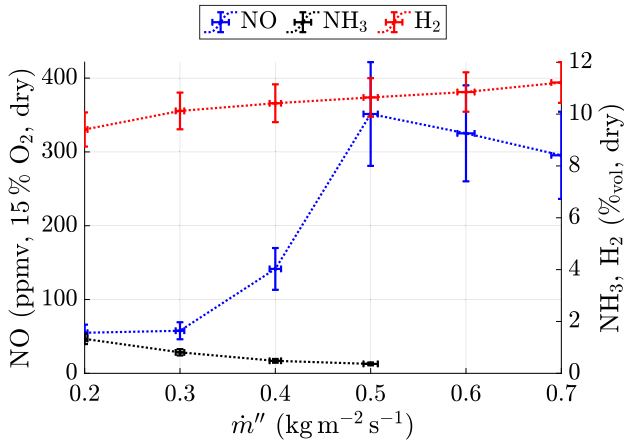
Fig. 9. Effect of mass flux on NO, NH$_3$ and H$_2$ emissions of the burner for fuel-rich operation, with $\phi = 1.3$ and $X_{NH_3} = 70\%$. Technical difficulties with the gas sampling system prevented unburnt NH$_3$ measurements beyond $\dot{m}'' = 0.5$ kg m^{-2} s^{-1}.
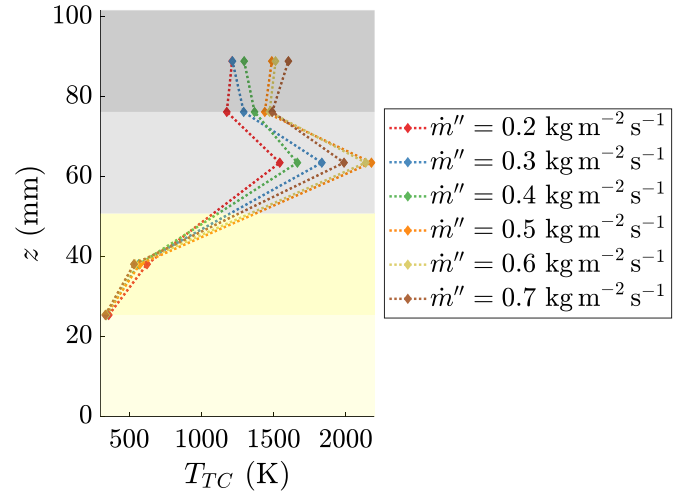
Fig. 10. Effect of operating parameters on thermocouple temperature during fuel rich operation: the mass flux is varied while the H$_2$ volume fraction in the fuel ($X_{NH_3} = 70\%$) and equivalence ratio ($\phi = 1.3$) are kept constant, matching conditions at which emissions are reported in Fig. 9.

analysis performed previously, this trend may be explained by higher heat recirculation and operating temperature in the PMB, especially on the downstream side of the burner, in the 10 PPI SiC foam (shown as dark grey in Fig. 10). NO emissions increase rapidly up to $\dot{m}'' = 0.5$ kg m^{-2} s^{-1}. This is associated with a rapid increase in the temperature in the 3 PPI foam ($z = 63.5$ mm), which reaches a maximum of 2178 K for $\dot{m}'' = 0.5$ kg m^{-2} s^{-1}. Further increasing $\dot{m}''$ yields a small decrease in both the peak temperature measured within the burner and NO emissions.

4. Conclusions

We investigated the matrix stabilized combustion of premixed NH$_3$/H$_2$/air mixtures by combining experiments in a porous media burner and a low-order reactor network model. An interface-stabilized burner design with a large pore size was used in order to avoid quenching of NH$_3$ flames with large thermal thicknesses. We demonstrated that this design is suitable to stabilize flames over a wide range of operating conditions, with, for the first time, an

experimental demonstration that PMBs can be used to stabilize pure NH_3/air flames. We found two additional practical benefits for NH_3 combustion in a PMB:

- a large turndown ratio of at least 15:1, comparable or in excess of state-of-the-art premixed hydrocarbon process burners [53];
- and a high volumetric power density of up to 62 MW m^{-3}, approximately three times greater than comparable swirl-stabilized NH_3 flames, which is advantageous for power generation and propulsion applications.

Extensive gas analysis measurements of NO, unburnt NH_3, and H_2 were conducted. A low-order reactor network model was developed, which includes interphase heat transfer and solid phase heat transfer. We found that this model predicted pollutant emissions of this burner to good accuracy, illustrating the importance of capturing heat recirculation and super-adiabaticity. We identified two combustion regimes most favorable for low NO emissions: lean combustion near the burner's extinction limit ($\phi \leq 0.55$) and rich combustion at $\phi \geq 1.2$. Rich combustion presented a significant difficulty as high levels of unburnt fuel remains in the exhaust stream. However, a large fraction of this unburnt fuel was in the form of H_2. We observed experimentally and confirmed through simulations that the reforming efficiency of the burner, and thus the amount of unburnt NH_3 in the exhaust stream, primarily depended on the burner's operating temperature. The burner mass flux affected residence time and burner temperature, and we found that this parameter had a second order effect on pollutant emissions: it slightly increased NO emissions but improved the reforming efficiency of NH_3 to H_2. Operation near the lean extinction limit provided NO emissions on the order of 100 ppmv, even though at this condition, high levels of H_2 blending ($X_{NH_3} \leq 70\%$) were necessary to stabilize the flame. Near the lean extinction limit, variable amounts of unburnt NH_3 were present in the exhaust stream. Emissions were generally on the order of 200 ppmv, but reached 20,000 ppmv at one condition. Further research is also necessary to quantify N_2O emissions, as these may be substantial at very lean conditions.

Although these results show the potential of PMBs as a practical solution for NH_3 fueled furnaces and gas turbines, further work is warranted to tailor porous foams for NH_3 combustion. Leveraging recent progress in ceramic additive manufacturing [33–35], topology gradation might allow to combine regions of large pore sizes required to stabilize NH_3/air flames, with finer pore regions more suitable for heat recirculation. The integration of catalysts onto the porous foam or the addition of exhaust gas post-treatment is another possible pathway for reducing pollutant emissions, and enabling a adoption of porous media combustion technology for NH_3 combustion.

Declaration of Competing Interest

The authors declare that they have no known competing financial interests or personal relationships that could have appeared to influence the work reported in this paper.

Appendix A. Temperature correction procedure for thermocouple measurements

Experimental temperature measurements within porous media burners are a challenging endeavor. In this work, we use 1 mm diameter Nicrotherm-sheathed type N thermocouples (TC Direct, Hillside, IL, USA). The relative accuracy of these thermocouples is 0.75%. The NI cDAQ acquisition system introduces an additional measurement uncertainty of ± 4 K on the measurement of the thermocouple's junction temperature. The reported temperatures are averaged over 2 min at a sampling rate of 1 Hz, leading to a statistical uncertainty of 5 K. As a non-platinum based thermocouple was used in the present study, catalytic effects are assumed to be negligible [59].

In our configuration, the main source of measurement uncertainties associated with the use of sheathed thermocouples within porous media burners is therefore the relationship between the temperature at the tip of the thermocouple and the temperatures of the solid and the gas, T_s and T_g. It is first useful to assess the level of homogeneity of the temperature field in the radial direction. Thermal losses at the outer cylindrical boundary are the dominant source of radial temperature gradient in the solid. To assess their importance, we use the following Biot number:

$$Bi = \frac{D\dot{q}_{loss}}{4(\lambda_{s,eff} + \lambda_{rad})(T_s - T_{amb})}. \tag{A.1}$$

The Biot number increases with the solid temperature T_s and reaches a value of $Bi = 0.1$ at $T_s = 2190$ K in the 10 PPI SiC foam. It is thus reasonable for our purpose to assume a uniform solid and gaseous temperature in the vicinity of the thermocouple. Conductive heat losses through the thermocouple's sheath, on the other hand, are a well known issue that must be compensated for in our setup [59]. We consider here the case of a cylindrical, 1D, sheathed thermocouple of outer diameter d_{TC} in steady state, inserted in a hot porous foam at a uniform temperature T_s over which a gas at T_g flows. This configuration is represented schematically in Fig. A1. The 1D heat transfer equation for the thermocouple reads:

$$\frac{d^2T}{dx^2} - \frac{4h_c}{d_{TC}\lambda_{TC}}(T - T_g) - \frac{4\sigma\varepsilon}{d_{TC}\lambda_{TC}}\left(T^4 - T_s^4\right) = 0, \tag{A.2}$$

where $T(x)$ is the local temperature of the thermocouple at position x, h_c is the conducto-convective heat transfer coefficient between the flowing gas and the cylindrical thermocouple, and λ_{TC} is the conductivity of the thermocouple. Following standard fin theory [60], this equation can be recast and linearized using
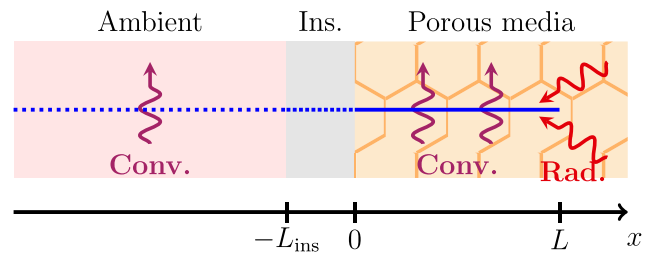

Fig. A1. Schematic of the model considered for thermocouple correction. The thermocouple is represented by a blue line. In the pink section (thermocouple shown as a dotted line, $x < -L_{ins}$), the thermocouple is surrounded by air at ambient conditions and cooled by natural convection; in the gray section (thermocouple shown as a densely dotted line, $-L_{ins} \leq x < 0$), the thermocouple is within the thermal insulation layer (Ins.) surrounding the porous media and is modeled as adiabatic; in the orange section (thermocouple shown a continuous line, $0 \leq x \leq L$), the thermocouple is within the porous media and is heated by natural convection from the surrounding gas and by radiation from the hot solid. (For interpretation of the references to colour in this figure legend, the reader is referred to the web version of this article.)
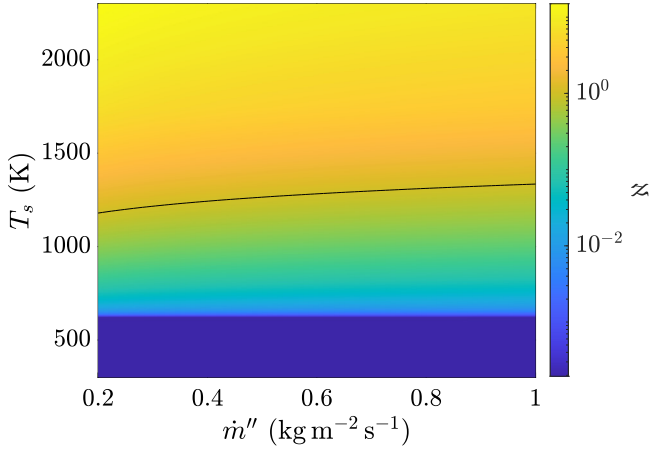
Fig. A2. ℵ (Eq. (A.3)), ratio between the radiative and convective source term in the thermocouple's energy balance equation. A black isocontour ℵ = 1 is shown for reference.

Fig. A3. Characteristic heat conduction length δ (Eq. (A.6)) as a function of burner operating parameters.

reduced temperatures $\theta_g = T - T_g$ and $\theta_s = T - T_s$, under the assumption $\theta_s \ll T_s$ in the ceramic foam:

$$\frac{d^2T}{dx^2} - \frac{4h_c}{d_{TC}\lambda_{TC}}\theta_g - \frac{16\sigma\epsilon T_s^3}{d_{TC}\lambda_{TC}}\theta_s = 0, \text{ for } x \geq 0. \quad (A.3)$$

The non-dimensional quantity

$$\aleph = \frac{4\sigma_{SB}\epsilon T_s^3}{h_c}, \quad (A.4)$$

a pseudo Nusselt number, thus quantifies the relative weight of radiative and convective heat transfer processes in the overall thermal balance of the thermocouple. h_c is estimated using a Nusselt number correlation for flow over a cylinder $Nu = 0.911Re^{0.385}Pr^{0.333}$ [60], with transport and thermal properties evaluated at the film temperature for a vitiated stoichiometric NH_3/air flow [43,44]. Radiative properties for high-nickel alloys from Balat-Pichelin et al. [61] are used. Figure A.2 shows that, in the hot, post-flame region of the burner, ℵ is on the order of unity, so that radiative and convective heat transfer processes are of similar magnitude. Following results by Zheng et al. [62], who found the temperature difference between solid and gas to be on the order of 10–20 K at steady state in the post flame region of their packed bead burner, we assume local quasi-thermal equilibrium: $\theta_g - \theta_s \ll \theta_s$, so that one may tentatively simplify Eq. (A.3) as

$$\frac{d^2\theta_s}{dx^2} - \frac{\theta_s}{\delta^2} = 0, \quad (A.5)$$

where the characteristic thermal length δ of the thermocouple is

$$\delta = \left[\frac{4}{d_{TC}\lambda_{TC}}\left(4\sigma\epsilon T_s^3 + h_c\right)\right]^{-0.5}. \quad (A.6)$$

Figure A.3 shows the dependency of δ to burner operating parameters. If $\delta \ll L$, then heat losses through the thermocouple sheath can be neglected. In the present work, δ and L are of similar order of magnitude, and Eq. (A.5) must be solved analytically. Because the ceramic foam is moving due to thermal expansion, thermal contact cannot be assured between a thermocouple and the hot ceramic foam. We therefore do not attempt to have contact between the thermocouple and the foam when installing them, and apply a convective/radiative flux boundary condition on the tip of the thermocouple ($x = L$):

$$\frac{d\theta_s}{dx}(x = L) = d_{TC}\delta^{-2}\theta_s(x = L), \quad (A.7)$$

and use a thermal resistance model at $x = 0$ (see Fig. A.1). The section of the thermocouple located in the thermal insulation layer

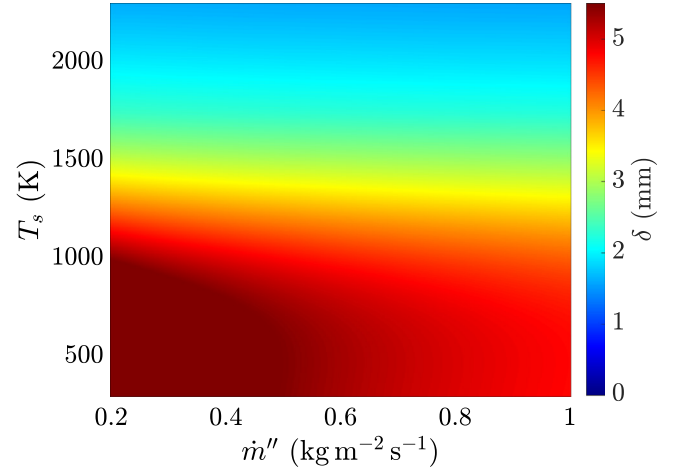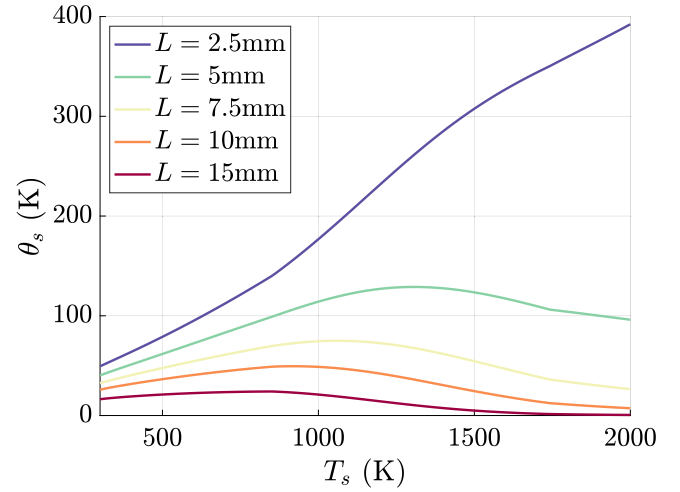**Fig. A4.** Temperature difference θ_s between the thermocouple junction and the solid/gas temperature in a porous foam as a function of the solid temperature T_s and the length of the inserted thermocouple L

is considered perfectly insulated, while the thermocouple's tail, located outside the burner, is modeled as an infinitely long cylindrical fin cooled by free convection in a quiescent ambient atmosphere [60]. Equating the heat flux on either side of the thermal insulation layer yields boundary conditions:

$$q(0) = q(-L_{ins}) = \lambda_{TC}\frac{d\theta_s}{dx}(0), \quad (A.8a)$$

$$q(0) = q(-L_{ins}) = \frac{\lambda_{TC}}{L_{ins}}(T(0) - T(-L_{ins})), \quad (A.8b)$$

$$q(0) = q(-L_{ins}) = \left(\frac{4h_{fcv}\lambda_{TC}}{d_{TC}}\right)^{0.5}(T(-L_{ins}) - T_{amb}). \quad (A.8c)$$

Equations (A.5)–(A.8c) are then solved analytically. Figure A.4 shows the temperature correction θ_s that must be applied to a measured thermocouple junction temperature. This is calculated for a stoichiometric NH_3/air vitiated flow. This analytical correction method, based on a local thermal equilibrium assumption, is used to correct all temperature measurements in the present work. Thermocouples inserted into the YZA foam ($z \leq 50.8$ mm) have a typical penetration length of $L \approx 3$ mm, while those inserted into

the SiC foams have a typical penetration length of $L \approx 8$ mm (3 PPI) and $L \approx 7$ mm (10 PPI). Considering the different sources of experimental uncertainties and the approximation made on local temperature non-equilibrium in deriving Eq. (A.5), we consider that the aggregated uncertainties on the reported temperature in the present work, outside of the flame zone itself, are ±50 K.

Supplementary material

Supplementary material associated with this article can be found, in the online version, at doi:10.1016/j.combustflame.2023. 112642

References

[1] International Panel on Climate Change, Contribution of Working Group II to the Sixth Assessment Report of the Intergovernmental Panel on Climate Change, in Climate Change 2022: Impacts, Adaptation, and Vulnerability, Cambridge University Press, 2022.

[2] F. Bird, A. Clarke, P. Davies, E. Surkovic, Ammonia: Fuel and Energy Store, Technical Report Policy Briefing DES5711, The Royal Society, 2020.

[3] N. Salmon, R. Bañares Alcántara, Green ammonia as a spatial energy vector: a review, Sustain. Energy Fuels 5 (11) (2021) 2814–2839, doi:10.1039/d1se00345c.

[4] A. Valera-Medina, F. Amer-Hatem, A.K. Azad, I.C. Dedoussi, M. de Joannon, R.X. Fernandes, P. Glarborg, H. Hashemi, X. He, S. Mashruk, J. McGowan, C. Mounaim-Rouselle, A. Ortiz-Prado, A. Ortiz-Valera, I. Rossetti, B. Shu, M. Yehia, H. Xiao, M. Costa, Review on ammonia as a potential fuel: from synthesis to economics, Energy Fuels 35 (9) (2021) 6964–7029, doi:10.1021/acs.energyfuels.0c03685.

[5] H. Kobayashi, A. Hayakawa, K.D.K.A. Somarathne, E.C. Okafor, Science and technology of ammonia combustion, Proc. Combust. Inst. 37 (1) (2019) 109–133, doi:10.1016/j.proci.2018.09.029.

[6] A.M. Elbaz, S. Wang, T.F. Guiberti, W.L. Roberts, Review on the recent advances on ammonia combustion from the fundamentals to the applications, Fuel Commun. 10 (2022) 100053, doi:10.1016/j.jfueco.2022.100053.

[7] C. Lhuillier, P. Brequigny, N. Lamoureux, F. Contino, C. Mounaïm-Rousselle, Experimental investigation on laminar burning velocities of ammonia/hydrogen/air mixtures at elevated temperatures, Fuel 263 (2020) 116653, doi:10.1016/j.fuel.2019.116653.

[8] O. Mathieu, E.L. Petersen, Experimental and modeling study on the high-temperature oxidation of ammonia and related NO_x chemistry, Combust. Flame 162 (3) (2015) 554–570, doi:10.1016/j.combustflame.2014.08.022.

[9] E.C. Okafor, K.D.K.A. Somarathne, A. Hayakawa, T. Kudo, O. Kurata, N. Iki, H. Kobayashi, Towards the development of an efficient low-NO_x ammonia combustor for a micro gas turbine, Proc. Combust. Inst. 37 (4) (2019) 4597–4606, doi:10.1016/j.proci.2018.07.083.

[10] A.A. Khateeb, T.F. Guiberti, X. Zhu, M. Younes, A. Jamal, W.L. Roberts, Stability limits and NO emissions of technically-premixed ammonia-hydrogen-nitrogen-air swirl flames, Int. J. Hydrog. Energy 45 (41) (2020) 22008–22018, doi:10.1016/j.ijhydene.2020.05.236.

[11] S. Mashruk, E.C. Okafor, M. Kovaleva, A. Alnasif, D.G. Pugh, A. Hayakawa, A. Valera-Medina, Evolution of N_2O production at lean combustion condition in NH_3/H_2/air premixed swirling flames, Combust. Flame 244 (2022) 112299, doi:10.1016/j.combustflame.2022.112299.

[12] M.C. Franco, R.C. Rocha, M. Costa, M. Yehia, Characteristics of NH_3/H_2/air flames in a combustor fired by a swirl and bluff-body stabilized burner, Proc. Combust. Inst. 38 (4) (2021) 5129–5138, doi:10.1016/j.proci.2020.06.141.

[13] E.C. Okafor, O. Kurata, H. Yamashita, T. Inoue, T. Tsujimura, N. Iki, A. Hayakawa, S. Ito, M. Uchida, H. Kobayashi, Liquid ammonia spray combustion in two-stage micro gas turbine combustors at 0.25 MPa; relevance of combustion enhancement to flame stability and NO_x control, Appl. Energy Combust. Sci. 7 (2021) 100038, doi:10.1016/j.jaecs.2021.100038.

[14] D. Pugh, P. Bowen, A. Valera-Medina, A. Giles, J. Runyon, R. Marsh, Influence of steam addition and elevated ambient conditions on NO_x reduction in a staged premixed swirling NH_3/H_2, Proc. Combust. Inst. 37 (4) (2019) 5401–5409, doi:10.1016/j.proci.2018.07.091.

[15] G.B. Ariemma, P. Sabia, G. Sorrentino, P. Bozza, M. de Joannon, R. Ragucci, Influence of water addition on MILD ammonia combustion performances and emissions, Proc. Combust. Inst. 38 (4) (2021) 5147–5154, doi:10.1016/j.proci.2020.06.143.

[16] X. Zhu, A.A. Khateeb, T.F. Guiberti, W.L. Roberts, NO and OH* emission characteristics of very-lean to stoichiometric ammonia-hydrogen-air swirl flames, Proc. Combust. Inst. 38 (4) (2021) 5155–5162, doi:10.1016/j.proci.2020.06.275.

[17] A. Valera-Medina, D.G. Pugh, P. Marsh, G. Bulat, P. Bowen, Preliminary study on lean premixed combustion of ammonia-hydrogen for swirling gas turbine combustors, Int. J. Hydrog. Energy 42 (38) (2017) 24495–24503, doi:10.1016/j.ijhydene.2017.08.028.

[18] G. Vignat, B. Akoush, E.R. Toro Garza, E. Boigné, M. Ihme, Combustion of lean ammonia-hydrogen fuel blends in a porous media burner, Proc. Combust. Inst. 40 (2023) Inpress, doi:10.1016/j.proci.2022.07.054.

[19] A.A. Khateeb, T.F. Guiberti, G. Wang, W.R. Boyette, M. Younes, A. Jamal, W.L. Roberts, Stability limits and NO emissions of premixed swirl ammonia-air flames enriched with hydrogen or methane at elevated pressures, Int. J. Hydrog. Energy 46 (21) (2021) 11969–11981, doi:10.1016/j.ijhydene.2021.01.036.

[20] E.C. Okafor, K.D.A. Somarathne, R. Ratthanan, A. Hayakawa, T. Kudo, O. Kurata, N. Iki, T. Tsujimura, H. Furutani, H. Kobayashi, Control of NO_x and other emissions in micro gas turbine combustors fuelled with mixtures of methane and ammonia, Combust. Flame 211 (2020) 406–416, doi:10.1016/j.combustflame.2019.10.012.

[21] G. Wang, T.F. Guiberti, S. Cardona, C.A. Jimenez, W.L. Roberts, Effects of residence time on the NOx emissions of premixed ammonia-methane-air swirling flames at elevated pressure, Proc. Combust. Inst. (2023) In press, doi:10.1016/j.proci.2022.07.141.

[22] J.L. Ellzey, E.L. Belmont, C.H. Smith, Heat recirculating reactors: fundamental research and applications, Prog. Energy Combust. Sci. 72 (2019) 32–58, doi:10.1016/j.pecs.2018.12.001.

[23] S. Wood, A.T. Harris, Porous burners for lean-burn applications, Prog. Energy Combust. Sci. 34 (5) (2008) 667–684, doi:10.1016/j.pecs.2008.04.003.

[24] A. Gharehghani, K. Ghasemi, M. Siavashi, S. Mehranfar, Applications of porous materials in combustion systems: a comprehensive and state-of-the-art review, Fuel 304 (2021) 121411, doi:10.1016/j.fuel.2021.121411.

[25] D. Mohaddes, C.T. Chang, M. Ihme, Thermodynamic cycle analysis of superadiabatic matrix-stabilized combustion for gas turbine engines, Energy 207 (2020) 118171, doi:10.1016/j.energy.2020.118171.

[26] S. Sobhani, J. Legg, D.F. Bartz, J.J. Kojima, C.T. Chang, J.D. Sullivan, J.P. Moder, M. Ihme, Experimental investigation of lean premixed pre-vaporized liquid-fuel combustion in porous media burners at elevated pressures up to 20 bar, Combust. Flame 212 (2020) 123–134, doi:10.1016/j.combustflame.2019.10.033.

[27] F.M. Pereira, A.A.M. Oliveira, F.F. Fachini, Maximum superadiabatic temperature for stabilized flames within porous inert media, Combust. Flame 158 (11) (2011) 2283–2288, doi:10.1016/j.combustflame.2011.04.001.

[28] P.A. Masset, O. Dounia, L. Selle, Fully explicit formulae for flame speed in infinite and finite porous media, Combust. Theory Model. 25 (5) (2021) 785–812, doi:10.1080/13647830.2021.1939422.

[29] C. Bedoya, I. Dinkov, P. Habisreuther, N. Zarzalis, H. Bockhorn, P. Parthasarathy, Experimental study, 1D volume-averaged calculations and 3D direct pore level simulations of the flame stabilization in porous inert media at elevated pressure, Combust. Flame 162 (2015) 3740–3754, doi:10.1016/j.combustflame.2015.07.012.

[30] J.C. Ferguson, S. Sobhani, M. Ihme, Pore-resolved simulations of porous media combustion with conjugate heat transfer, Proc. Combust. Inst. 38 (2) (2021) 2127–2134, doi:10.1016/j.proci.2020.06.064.

[31] A. Bakry, A. Al-Salaymeh, A.H. Al-Muhtaseb, A. Abu-Jrai, D. Trimis, Adiabatic premixed combustion in a gaseous fuel porous inert media under high pressure and temperature: novel flame stabilization technique, Fuel 90 (2) (2011) 647–658, doi:10.1016/j.fuel.2010.09.050.

[32] F. Song, Z. Wen, Z. Dong, E. Wang, X. Liu, Ultra-low calorific gas combustion in a gradually-varied porous burner with annular heat recirculation, Energy 119 (2017) 497–503, doi:10.1016/j.energy.2016.12.077.

[33] S. Sobhani, S. Allan, P. Muhunthan, E. Boigne, M. Ihme, Additive manufacturing of tailored macroporous ceramic structures for high-temperature applications, Adv. Eng. Mater. 22 (8) (2020) 1–8, doi:10.1002/adem.202000158.

[34] S. Sobhani, P. Muhunthan, E. Boigné, D. Mohaddes, M. Ihme, Experimental feasibility of tailored porous media burners enabled via additive manufacturing, Proc. Combust. Inst. 38 (4) (2021) 6713–6722, doi:10.1016/j.proci.2020.06.120.

[35] M. Pelanconi, A. Ortona, Review on the design approaches of cellular architectures produced by additive manufacturing, Industrializing Additive Manufacturing, Springer International Publishing (2021), pp. 52–64, doi:10.1007/978-3-030-54334-1.

[36] R.C. Rocha, C.F. Ramos, M. Costa, X.S. Bai, Combustion of NH_3/CH_4/air and NH_3/H_2/air mixtures in a porous burner: experiments and kinetic modeling, Energy Fuels 33 (12) (2019) 12767–12780, doi:10.1021/acs.energyfuels.9b02948.

[37] H. Nozari, G. Karaca, O. Tuncer, A. Karabeyoglu, Porous medium based burner for efficient and clean combustion of ammonia-hydrogen-air systems, Int. J. Hydrog. Energy 42 (21) (2017) 14775–14785, doi:10.1016/j.ijhydene.2017.03.234.

[38] D. Trimis, F. Durst, Combustion in a porous medium: advances and applications, Combust. Sci. Technol. 121 (1–6) (1996) 153–168, doi:10.1080/00102209608935592.

[39] N. Otsu, Threshold selection from gray-level histograms, IEEE Trans. Syst., Man, Cybern. SMC-9 (1) (1979) 62–66, doi:10.1109/tsmc.1979.4310076.

[40] E. Maire, P. Colombo, J. Adrien, L. Babout, L. Biasetto, Characterization of the morphology of cellular ceramics by 3D image processing of X-ray tomography, J. Eur. Ceram. Soc. 27 (4) (2007) 1973–1981, doi:10.1016/j.jeurceramsoc.2006.05.097.

[41] J. Gostick, Z. Khan, T. Tranter, M. Kok, M. Agnaou, M. Sadeghi, R. Jervis, et al., PoreSpy: a Python toolkit for quantitative analysis of porous media images, J. Open Source Softw. 4 (37) (2019) 1296, doi:10.21105/joss.01296.

[42] C.E. Baukal, P.B. Eleazer, Quantifying NO_x for industrial combustion processes, J. Air Waste Manag. Assoc. 48 (1) (1998) 52–58, doi:10.1080/10473289.1998.10463664.

[43] D.G. Goodwin, R.L. Speth, H.K. Moffat, B.W Weber, Cantera: an object-oriented software toolkit for chemical kinetics, thermodynamics, and transport processes, (2021) URL https://www.cantera.or

[44] A. Stagni, C. Cavallotti, S. Arunthanayothin, Y. Song, O. Herbinet, F. Battin-Leclerc, T. Faravelli, An experimental, theoretical and kinetic-modeling study of the gas-phase oxidation of ammonia, React. Chem. Eng. 5 (4) (2020) 696–711, doi:10.1039/c9re00429g.

[45] A. Szanthoffer, Chemical Kinetic Modeling of the Combustion of NH_3/H_2 and NH_3/Syngas Fuel Mixtures Using a Large Amount of Experimental Data, Lund University, 2022 Master's thesis. http://lup.lub.lu.se/student-papers/record/9082232.

[46] A. Alnasif, S. Mashruk, M. Hayashi, A. Hayakawa, A. Valera-Medina, Performance investigation of currently available reaction mechanisms in the estimation of NO measurements: a comparative study, presented at the 1st Symposium on Ammonia Energy, Cardiff, Wales, United Kingdom (2022).

[47] O. Nilsson, H. Mehling, R. Horn, J. Fricke, R. Hofmann, S.G. Müller, R. Eckstein, D. Hofmann, Determination of the thermal diffusivity and conductivity of monocrystalline silicon carbide (300–2300 K), High Temp. - High Press. 29 (1) (1997) 73–79, doi:10.1068/htec142.

[48] G.A. Slack, Thermal conductivity of pure and impure silicon, silicon carbide, and diamond, J. Appl. Phys. 35 (12) (1964) 3460–3466, doi:10.1016/S0375-9601(98)00347-8.

[49] W. Chase Malcolm Jr., NIST-JANAF thermochemical tables, fourth edition, J. Phys. Chem. Ref. Data 62 (1998) 1–1951, doi:10.1021/ac00212a751.

[50] J.R. Howell, M.P. Mengüç, K. Daun, R. Siegel, Thermal Radiation Heat Transfer, CRC Press, 2020.

[51] P.F. Hsu, J.R. Howell, Measurements of thermal conductivity and optical properties of porous partially stabilized zirconia, Exp. Heat Transf. 5 (4) (1992) 293–313, doi:10.1080/08916159208946446.

[52] Y. Ju, B. Xu, Effects of channel width and lewis number on the multiple flame regimes and propagation limits in mesoscale, Combust. Sci. Technol. 178 (10–11) (2006) 1723–1753, doi:10.1080/00102200600788643.

[53] Riello, Product catalog for process burners, 2021. https://www.riello.com/international/files/catalogo-pdf/riello_products_catalogue_international-markets_process_burners_eng.pdf.

[54] J. Choe, W. Sun, T. Ombrello, C. Carter, Plasma assisted ammonia combustion: simultaneous NO_x reduction and flame enhancement, Combust. Flame 228 (2021) 430–432, doi:10.1016/j.combustflame.2021.02.016.

[55] A. Valera-Medina, M. Gutesa, H. Xiao, D. Pugh, A. Giles, B. Goktepe, R. Marsh, P. Bowen, Premixed ammonia/hydrogen swirl combustion under rich fuel conditions for gas turbines operation, Int. J. Hydrog. Energy 44 (16) (2019) 8615–8626, doi:10.1016/j.ijhydene.2019.02.041.

[56] O. Elishav, B. Mosevitzky Lis, E.M. Miller, D.J. Arent, A. Valera-Medina, A. Grinberg Dana, G.E. Shter, G.S. Grader, Progress and prospective of nitrogen-based alternative fuels, Chem. Rev. 120 (12) (2020) 5352–5436, doi:10.1021/acs.chemrev.9b00538.

[57] R.V. Fursenko, I.A. Yakovlev, E.S. Odintsov, S.D. Zambalov, S.S. Minaev, Pore-scale flame dynamics in a one-layer porous burner, Combust. Flame 235 (2022) 111711, doi:10.1016/j.combustflame.2021.111711.

[58] F. Sirotkin, R.V. Fursenko, S. Kumar, S. Minaev, Flame anchoring regime of filtrational gas combustion: theory and experiment, Proc. Combust. Inst. 36 (3) (2017) 4383–4389, doi:10.1016/j.proci.2016.06.006.

[59] M.V. Heitor, A.L.N. Moreira, Thermocouples and sample probes for combustion studies, Prog. Energy Combust. Sci. 19 (3) (1993) 259–278, doi:10.1016/0360-1285(93)90017-9.

[60] T.L. Bergman, F.P. Incropera, D.P. Dewitt, A.S. Lavine, Fundamentals of Heat and Mass Transfer, John Wiley & Sons, 2011.

[61] M. Balat-Pichelin, J.L. Sans, E. Bêche, L. Charpentier, A. Ferrière, S. Chomette, Emissivity at high temperature of Ni-based superalloys for the design of solar receivers for future tower power plants, Sol. Energy Mater. Sol. Cells 227 (July 2020) (2021) 111066, doi:10.1016/j.solmat.2021.111066.

[62] C. Zheng, L. Cheng, A. Saveliev, Z. Luo, K. Cen, Gas and solid phase temperature measurements of porous media combustion, Proc. Combust. Inst. 33 (2) (2011) 3301–3308, doi:10.1016/j.proci.2010.05.037.